https://doi.org/10.5194/egusphere-2026-6656
Preprint. Discussion started: 9 November 2026
© Author(s) 2026. CC BY 4.0 License.

Afternoon and nighttime differences in IRI-2026 electron-content partitioning over Hainan

Zheng Wang[1,2], Quanhan Li[1], Zehao Wang[3]*, Qinzeng Li[1,2], Yajun Zhu[1,2], Guojun Wang[1,2], Yusen Tian[4], and Xiao Wang[1,2]

[1] State Key Laboratory of Solar Activity and Space Weather, National Space Science Center, Chinese Academy of Sciences, Beijing, China
[2] National Field Observation and Research Station (Hainan) for Space Weather, Hainan, China
[3] National Key Laboratory of Scattering and Radiation, China Aerospace Science and Technology Corporation, 365 Zhayin Road, Yangpu District, Shanghai, China
[4] Beijing Key Laboratory of Space Environment Exploration, National Space Science Center, Chinese Academy of Sciences, Beijing, China

Correspondence: Zehao Wang (wangzehao1991@163.com)

Abstract

Does replacing the modeled bottomside with a locally observed profile improve total electron content (TEC) estimates? We examine this question at Hainan using 1,666 manually traced ionosonde profiles from 852 dates in 2015-2018 and the International Reference Ionosphere (IRI-2026). We replace the modeled profile below the F2 density peak with the traced bottomside, retain the modeled topside to 1000 km, and compare the original and combined columns with contemporaneous GNSS vertical TEC. Replacement increases overall mean absolute error from 5.064 to 5.898 TECU, but the two sampled local times respond differently. Error rises from 6.305 to 8.440 TECU in the afternoon and falls from 3.808 to 3.325 TECU after midnight. Under their respective integration limits, the modeled afternoon bottomside contains 4.338 TECU more than the traced bottomside on average. This extra lower-column content partly offsets the positive GNSS-minus-combined difference, making the original total closer to GNSS. The opposite responses persist when the two integrals meet at the observed peak height. At Hainan, closer agreement in total TEC can therefore conceal a substantial difference in the lower profile, and introducing that observed profile can expose the discrepancy. These Hainan results show that regional TEC updating needs to assess the upper contribution alongside the observed bottomside, particularly in the afternoon, while accounting for GNSS electron content above 1000 km.

1 Introduction

A local measurement can improve the description of one part of the ionosphere while leaving the total electron content (TEC) farther from observations. This matters when combining ground-based ionosonde profiles with a global model. An ionosonde constrains the F-region peak and the profile below it; GNSS measures electron

https://doi.org/10.5194/egusphere-2026-6656
Preprint. Discussion started: 9 November 2026
© Author(s) 2026. CC BY 4.0 License.

content integrated along a much longer path. TEC determines the first-order GNSS propagation delay (Mannucci et al., 1998), while studies of vertical plasma structure also require density as a function of height. At a station with both instruments, the measured bottomside and GNSS TEC allow us to ask whether using the local lower profile also improves the modeled column.

The International Reference Ionosphere (IRI) provides a global empirical description of monthly-average ionospheric conditions, assembled from ground-based and satellite observations. It specifies peak parameters and density variation below and above the F2 peak (Bilitza et al., 2014, 2022). Its climatological background supports applications where observations are sparse, but local production, loss, and transport produce departures in both profile amplitude and shape. Pignalberi et al. (2025) found that IRI-2020 tended to underestimate large altimeter-derived TEC values, with performance depending on magnetic latitude, local time, and season. For regional use, identifying the profile contributions to such differences is as important as measuring the total discrepancy.

Separating those contributions has a substantial observational basis. Belehaki and Kersley (2006) tested bottomside-based TEC reconstruction against incoherent scatter radar (ISR) profiles and found better agreement at night than during daytime. Bidaine and Warnant (2007) combined ionosonde and GPS information to examine NeQuick's lower and upper columns, including a case in which their opposing differences nearly cancelled in the total. Themens et al. (2021) likewise showed that interacting peak and topside errors can help or hinder agreement with TEC. These studies establish why a close column integral can coexist with an inaccurate vertical distribution. They also motivate evaluating what happens when a measured lower profile replaces one of the modeled contributions.

Recent work has constrained the upper region more directly. Pignalberi et al. (2026) used ionosonde peak parameters and collocated radio-occultation profiles to compare IRI-2020 topside options, finding IRI-COR2 the best overall low-latitude option in their profile comparison. Servan-Schreiber et al. (2025), using ionosonde-driven IRI and ground GNSS TEC, instead found smaller low-latitude TEC errors with NeQuick than with the tested COR2 combinations. The measurements, altitude coverage, and model inputs differ, so the two assessments address different aspects of performance. For a station with bottomside profiles and GNSS TEC, an important practical issue is how the local lower constraint changes the agreement of the combined column when the upper model is held fixed.

Hainan already has a history of such complementary observations. Zhang et al. (2006) compared IRI, GPS-IGS, and ionogram-derived TEC there and documented local-time differences; Wang et al. (2010) evaluated the

https://doi.org/10.5194/egusphere-2026-6656
Preprint. Discussion started: 9 November 2026
© Author(s) 2026. CC BY 4.0 License.

NeQuick bottomside thickness parameter using Hainan profiles. These studies establish regional departures in column estimates and lower-profile structure. In the equatorial ionization anomaly, daytime plasma uplift and field-aligned redistribution can change the relation between peak density and vertical content (Balan et al., 2018). Hainan observations also document plasma bubbles and strong range spread F (Wang et al., 2015). Afternoon and post-midnight observations therefore provide physically distinct conditions in which to examine the consequences of replacing the modeled lower column with its observed counterpart.

Here we combine Hainan profiles from 2015-2018 with contemporaneous GNSS TEC and IRI-2026. We test whether replacing the model bottomside improves the column estimate in the afternoon and after midnight, then use the lower and upper contributions to explain the difference. A comparison at a common peak height tests whether the result depends on where the two profiles meet. Associations with peak density and height provide additional context for the remaining TEC difference. The aim is to identify when local bottomside information can improve a Hainan column estimate and when the upper contribution also needs adjustment.

2 Data and methods

2.1 Site, observations, and comparison design

To examine whether a locally constrained bottomside is compatible with the modeled upper column, we compare the original IRI total and an observed-bottomside plus IRI-topside combination against the same GNSS reference. The individual ionosonde profile is the comparison unit. Separating afternoon and nighttime samples tests whether the benefit of using local observations changes with the background ionospheric state.

We used ionosonde profiles and GNSS TEC from Fuke, Hainan, in 2015-2018. The Meridian Project product-name correspondence identifies the historical Fuke station as Danzhou in the current catalogue; the GNSS input files use station code ODAZH (Chinese Meridian Project, n.d.-e). The representative GNSS antenna position is 19.527° N, 109.134° E, with a WGS84 height of 92 m. At the reference epoch of 2 July 2017, IGRF-14 gives a centered-dipole latitude of 10.0° N, an inclination of 28.0°, and an inclination-derived dip latitude of 14.9° N (Beggan et al., 2026). The IRI calculations use 19.5° N, 109.1° E.

The profile archive contains manually traced SAO43 electron-density profiles and their associated foF2 and hmF2 parameters. All eligible profiles at 06:00 and 18:00 UTC were retained. At the model longitude, these times correspond approximately to 13:16 and 01:16 local solar time. We refer to them as the afternoon and nighttime samples. The comparison contains 1,666 profiles on 852 UTC dates, including 814 dates with both

https://doi.org/10.5194/egusphere-2026-6656
Preprint. Discussion started: 9 November 2026
© Author(s) 2026. CC BY 4.0 License.

slots. The fixed slots provide a repeatable comparison of sunlit and post-midnight conditions across the available dates.

The observational products originate from the Chinese Meridian Project. The ionospheric-parameter and vertical absolute TEC records are identified by Chinese Meridian Project (n.d.-b, n.d.-c). RINEX data provide GNSS source provenance (Chinese Meridian Project, n.d.-d); we used the existing processed TEC product rather than performing a new RINEX inversion. The image product supplies the spread-F classification lineage (Chinese Meridian Project, n.d.-a). The local profile and GNSS columns are held identical in the IRI-2026 and historical model comparisons.

2.2 Bottomside profiles and coincident GNSS TEC

The manually traced profiles provide a lower-column constraint that retains the shape of the observed ionogram. Experienced researchers inspected and edited the ordinary-mode (O-mode) frequency-virtual-height trace in SAO Explorer. For ambiguous spread-F traces, interpretation used preceding and following ionograms together with continuous points in the current image, or followed the lower envelope of the red O-mode echo. SAO Explorer provides interactive trace editing and invokes the NHPC true-height inversion to obtain electron density as a function of true height (UMLCAR, n.d.-a). The archived processing headers document SAO Explorer 3.4.17 and NH 4.34. Virtual height includes radio-wave group delay; the inversion converts the edited trace to a height-density profile rather than treating the displayed echo height as the reflection altitude.

The resulting SAO 4.3 files store corresponding true-height, plasma-frequency, and electron-density arrays in groups 51-53 (UMLCAR, n.d.-b). We use the existing exports to obtain the observed lower column. This provides information about bottomside thickness and shape in addition to foF2 and hmF2. It is this additional vertical information that enables the component comparison: profiles with similar peaks can contain different amounts of plasma below the peak.

For each manually traced profile, the observed bottomside column, B_m, is the trapezoidal integral of electron density from its lowest reported height to the first density maximum. Thus the lower integration boundary follows the available profile, and no unobserved lower-altitude contribution is filled. Only the bottomside portion is used, because the ground-based sounding constrains the profile below the peak and the exported upper extension depends on a model. With density in cm^{-3} and height in km, the integral is multiplied by 10^{-7} to obtain TECU.

https://doi.org/10.5194/egusphere-2026-6656
Preprint. Discussion started: 9 November 2026
© Author(s) 2026. CC BY 4.0 License.

Profiles were required to contain at least 20 aligned height, frequency, and density points, with increasing heights, finite nonnegative densities, and a maximum relative frequency-density discrepancy of 0.015. Coincident GNSS and model-component values also had to be finite. Selection did not depend on the resulting TEC residual. Further catalogue and parameter-matching details are given in Appendix A.

To compare the local bottomside with a contemporaneous full column, the GNSS reference column, G, is the median of the cross-satellite epoch medians within $[t - 7.5\text{min}, t + 7.5\text{min})$, where t is the ionosonde time. The input is the Meridian Project L2 vertical absolute TEC product from GNSS monitor GTSM02. A checked source-file header identifies version V01.00, a nominal 30 s sampling interval, a 450 km thin-shell height, and Harbin Institute of Technology, Shenzhen, as producer. Our preprocessing removes unparsable records and the documented missing-value flags before aggregation. It adds no elevation-angle cutoff, slant-to-vertical mapping, or receiver-bias adjustment. The two medians summarize the available satellite paths around the station, whose spatial coverage differs from the ionosonde sounding. Supplement S2 separates these processing steps from the product metadata.

Spread-F classes were obtained from the image-classification method of Wang et al. (2023): no spread F, frequency spread F (FSF), range spread F (RSF), strong range spread F (SSF), and mixed spread F (MSF). They are used for descriptive stratification and statistical adjustment. The classes and manually traced electron-density profiles are separate inputs.

2.3 IRI profiles and column definitions

We separate IRI into lower and upper contributions to determine which part of the column changes when local bottomside information is introduced. Retaining the IRI topside isolates the response to bottomside replacement under the chosen integration definitions; the common-height comparison below examines the influence of the splice.

IRI-2026 was evaluated at the original UTC times using the official Fortran distribution (IRI Working Group, 2026). The configuration uses URSI foF2, Shubin-COSMIC hmF2, ABT-2009 bottomside parameters, IRI-COR2 topside, and the Ozhogin plasmasphere option without a plasmapause. Solar and geomagnetic index files were retained from the historical calculation. All model column integrations in this study end at 1000 km, including those for which a plasmasphere option is enabled.

The model density grid extends from 80 to 1000 km at 10 km intervals. In the primary comparison, the bottomside column B_I sums grid points at or below model hmF2, and the topside column T_I sums points above it.

https://doi.org/10.5194/egusphere-2026-6656
Preprint. Discussion started: 9 November 2026
© Author(s) 2026. CC BY 4.0 License.

For density in m^{-3}, multiplying each sum by 10^{-12} gives TECU. The original model total, C_I, is obtained separately through native IRITEC integration from 0 to 1000 km with a configured 0.1 km step. The component sums and native total are therefore distinct numerical estimates.

The hybrid column and its remaining TEC are

$$H = B_m + T_I, R = G - H. \quad (1)$$

The original model residual is $R_I = G - C_I$. Positive R means that GNSS TEC exceeds the combined observed-bottomside and modeled-topside content. Because GNSS samples a greater altitude range, R includes contributions outside the model interval as well as observational and profile differences within it.

To relate the component comparison to the original-model residual, define the numerical total-component difference as δ:

$$\delta = C_I - (B_I + T_I), R_I = R - (B_I - B_m) - \delta. \quad (2)$$

This identity shows how a larger modeled lower contribution can offset a positive hybrid residual. The difference $B_I - B_m$ includes the different lower boundaries and peak heights of the two integrals. It describes the columns used in the comparison; MAE is evaluated separately after taking the absolute value for each profile.

The historical comparison uses iri2020 Python-wrapper outputs for the same observations. It is labeled IRI-2020 (historical) throughout. Using the same observations in both configurations helps locate the model contribution responsible for a change in the hybrid column. The foF2 difference uses the model quiet-reference value, whereas the density profile can include the configured storm response. Appendix A gives the numerical details needed to interpret this distinction.

2.4 Statistical comparisons

All errors are measured relative to the contemporaneous GNSS vertical TEC, G, defined in Sect. 2.2. For the same n matched profiles, the original-model and hybrid mean absolute errors (MAEs) are

$$\mathrm{MAE}_I = \frac{1}{n}\sum_{i=1}^{n} |C_{I,i} - G_i|, \mathrm{MAE}_H = \frac{1}{n}\sum_{i=1}^{n} |H_i - G_i|. \quad (3)$$

Each profile has equal weight; subgroup MAEs use the profiles within that group. GNSS TEC serves as an observational reference with measurement and spatial-sampling uncertainty. The median and positive fraction of the signed residual describe the direction of the column difference. Relative MAE improvement is

https://doi.org/10.5194/egusphere-2026-6656
Preprint. Discussion started: 9 November 2026
© Author(s) 2026. CC BY 4.0 License.

$$I = I - \frac{mean(|R|)}{mean(|R_I|)}. \quad (4)$$

Negative I denotes worsening. Overall median and relative-improvement confidence intervals use 2,000 bootstrap samples of UTC dates, retaining both profiles together when present. The limits are the 2.5th and 97.5th percentiles. Year, season, time-slot, and morphology summaries show where the pooled response is concentrated. To compare the two time sectors on the same set of dates, we use the 814 dates with both slots. Their paired contrast is $R(18\text{UTC}) - R(06\text{UTC})$, evaluated with a two-sided Wilcoxon signed-rank test.

To examine whether column disagreement accompanies departures in peak density or peak height, three ordinary-least-squares models describe R, $|R|$, and $|R_I| - |R|$. The first uses observed-minus-IRI foF2 and hmF2; the other two use absolute peak-parameter differences. Continuous predictors are standardized using their sample population standard deviations. All models adjust for UTC slot, year, season, and SF class. Confidence intervals use covariance estimates clustered by UTC date. The specifications, reference levels, and multiple-testing procedure are given in Appendix A. The signed model distinguishes a larger remaining column from a smaller one; the two absolute-error models describe mismatch magnitude and the benefit of replacement. The covariates adjust for the recorded differences in time sector, year, season, and morphology.

2.5 Common-height comparison

The observed and modeled density peaks may occur at different heights. Combining their independently defined lower and upper integrals can therefore leave an altitude gap or overlap. To examine its contribution, we use the existing piecewise-linear IRI profiles to integrate first from model hmF2 and then from the observed density-peak height to 1000 km. This also distinguishes the change in quadrature from the change in splice height. The manual bottomside retains its original lower boundary and content, and the GNSS column remains unchanged. Thus this calculation aligns the splice at the peak while retaining the unfilled region below the first reported manual height.

This comparison tests whether the afternoon and nighttime responses persist when the upper integral starts at the observed peak height. It uses the existing profiles without extrapolation or fitted correction.

3 Results

3.1 Total-column agreement

Replacing the IRI-2026 bottomside with the observed profile increases the overall MAE relative to GNSS vertical TEC, from 5.064 to 5.898 TECU (Tables 1 and S2). This corresponds to a 16.5% increase, with a date-clustered 95% interval of 13.2%-19.9%. The historical IRI-2020 combination gives the opposite response: MAE

https://doi.org/10.5194/egusphere-2026-6656
Preprint. Discussion started: 9 November 2026
© Author(s) 2026. CC BY 4.0 License.

decreases from 5.297 to 3.965 TECU, an improvement of 25.1% (95% interval 22.6%-27.5%). The original IRI-2026 total has a slightly smaller MAE than the historical total, even though its hybrid performs less well.

Table 1. Total-column agreement for the same 1,666 profiles on 852 dates. MAE is calculated against the same contemporaneous GNSS vertical TEC for both columns; errors and remaining columns are in TECU. Brackets denote date-clustered bootstrap 95% intervals. Relative improvement is a fraction; negative values indicate worsening. Both model integrations end at 1000 km.

Statistic	IRI-2020 (historical)	IRI-2026
Raw IRI MAE (TECU)	5.297	5.064
Hybrid MAE (TECU)	3.965	5.898
Remaining-column mean (TECU)	1.973	5.766
Remaining-column median (TECU)	2.111 [1.970, 2.260]	4.287 [4.087, 4.440]
Relative MAE improvement (fraction)	0.251 [0.226, 0.275]	-0.165 [-0.199, -0.132]
Positive remaining-column fraction	0.717	0.959

Figure 1 shows that the IRI-2026 response differs between the two time slots. In the afternoon, replacement increases MAE from 6.305 to 8.440 TECU. At night, it decreases MAE from 3.808 to 3.325 TECU. The two samples are similar in size, with 838 and 828 profiles, respectively, so the pooled worsening combines a larger afternoon loss with a smaller nighttime benefit. Local bottomside replacement therefore has a time-dependent value for reconstructing the column at this station.

https://doi.org/10.5194/egusphere-2026-6656
Preprint. Discussion started: 9 November 2026
© Author(s) 2026. CC BY 4.0 License.

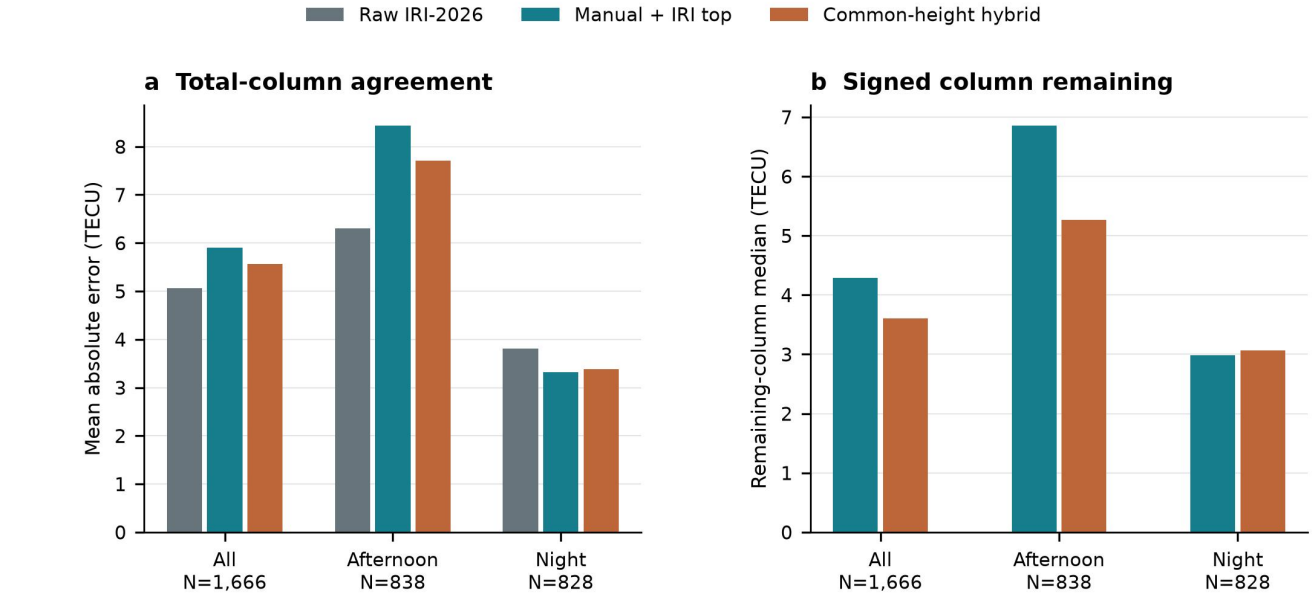


Figure 1. IRI-2026 total-column comparison. (a) MAE relative to GNSS TEC for the original model, the observed-bottomside plus model-topside hybrid, and the common-height hybrid. (b) Median GNSS-minus-hybrid TEC. The common-height calculation starts the IRI upper integral at the observed peak; all model integrals end at 1000 km. Afternoon and night denote 06:00 and 18:00 UTC. Counts are profiles; the full sample covers 852 dates.

Table 2 provides the year and morphology summaries. Table S3 also includes the time-slot and season summaries. Replacement worsens MAE in 2016-2018 and changes it little in 2015. Each SF class has a smaller hybrid than original MAE, whereas the no-SF group has a larger hybrid MAE. These group summaries retain their observed local-time and seasonal composition. Section 3.5 examines morphology-related associations with the signed residual after covariate adjustment.

Table 2. IRI-2026 results by year and SF morphology. The two blocks partition the same sample in different ways; a date may occur in more than one morphology group. All column values are in TECU. FSF, RSF, SSF, and MSF denote frequency, range, strong-range, and mixed spread F.

Stratum	Profiles	Dates	Raw MAE	Hybrid MAE	Remaining median
2015	149	77	9.836	9.801	6.052
2016	712	363	5.602	6.369	4.687
2017	256	129	4.936	6.692	5.373
2018	549	283	3.131	3.857	3.289

https://doi.org/10.5194/egusphere-2026-6656
Preprint. Discussion started: 9 November 2026
© Author(s) 2026. CC BY 4.0 License.

Stratum	Profiles	Dates	Raw MAE	Hybrid MAE	Remaining median
No SF	1265	826	5.329	6.542	4.767
FSF	147	147	3.186	3.008	2.770
RSF	125	121	5.245	4.728	4.110
SSF	35	35	8.190	7.320	5.268
MSF	94	94	3.031	2.774	2.688

3.2 Remaining TEC and the same-date contrast

GNSS TEC usually exceeds the hybrid estimate. The remaining column has a median of 4.287 TECU (95% interval 4.087-4.440 TECU), and 95.9% of values are positive. Its median is 6.861 TECU in the full afternoon group and 2.982 TECU at night (Fig. 1b).

The 814 dates containing both profiles also show a larger afternoon remaining column (Table 3). Their median paired nighttime-minus-afternoon difference is -4.091 TECU (Wilcoxon statistic 29,494; $p = 8.46 \times 10^{-92}$). The marginal medians within this paired subset are 6.871 and 2.982 TECU. The larger afternoon discrepancy persists when the two sectors are compared on the same dates, supporting a local-time difference beyond the unequal availability of the two slots (Table S4).

Table 3. Same-UTC-date contrast in remaining TEC, using 814 dates and 1,628 profiles for each configuration. Differences are 18 UTC minus 06 UTC. The median paired difference is distinct from the difference of marginal medians. Column values are in TECU.

Statistic	IRI-2020 (historical)	IRI-2026
06 UTC remaining median (TECU)	0.260	6.871
18 UTC remaining median (TECU)	2.587	2.982
Median paired difference (TECU)	2.478	-4.091
Mean paired difference (TECU)	1.332	-5.095
Positive paired-difference fraction	0.636	0.179
Wilcoxon statistic (p value)	115014 (p=3.560e-14)	29494 (p=8.456e-92)

3.3 Lower and upper contributions

Figure 2 separates the model columns and their relation to the observed bottomside (Table S5). Across all profiles, the modeled topside mean changes from 14.493 TECU in the historical calculation to 10.700 TECU in IRI-2026,

https://doi.org/10.5194/egusphere-2026-6656
Preprint. Discussion started: 9 November 2026
© Author(s) 2026. CC BY 4.0 License.

a difference of -3.793 TECU. The corresponding bottomside means are similar, at 9.481 and 9.502 TECU. The topside change is much larger in the afternoon (-6.985 TECU) than at night (-0.561 TECU).

Under their respective integration limits, the afternoon IRI-2026 bottomside exceeds the observed bottomside by an average of 4.338 TECU (Fig. 2b). At night, the mean difference is -0.416 TECU. The larger modeled afternoon bottomside therefore offsets part of the positive column remaining above the hybrid estimate. The mean difference between the native IRI total and the coarse bottom-plus-top sum is -0.029 TECU over the full sample. This is a pooled signed difference, whereas MAE depends on the distribution of individual residuals. The bottomside contrast describes the contribution removed by replacement; its mean is not a direct allocation of the MAE change.

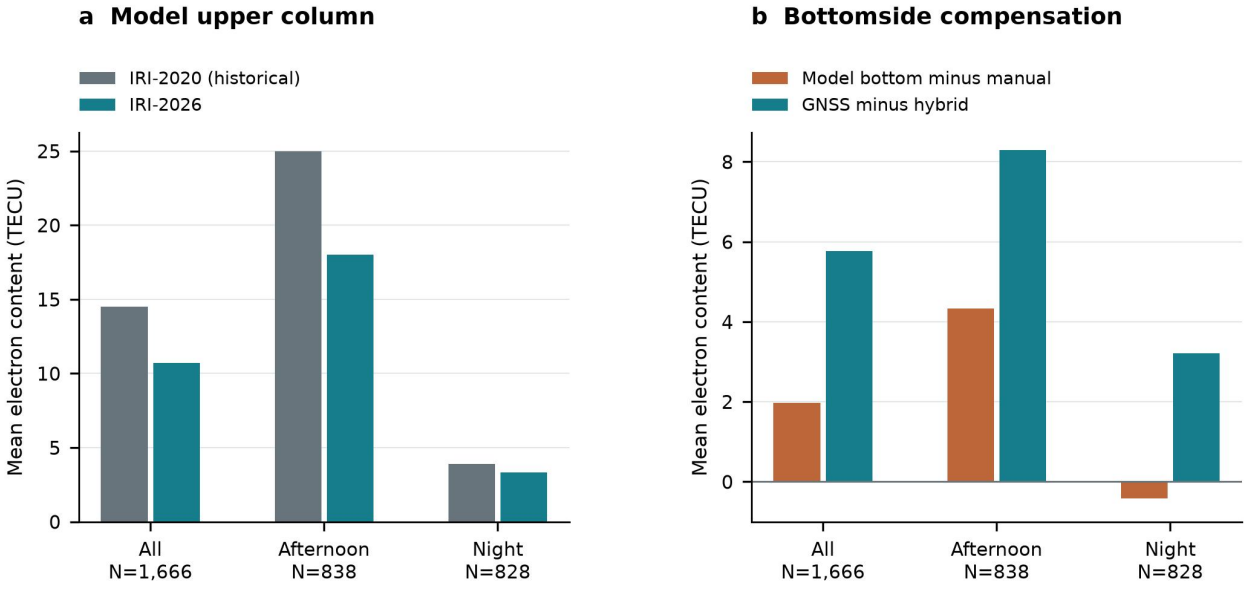


Figure 2. Model components and bottomside compensation. (a) Mean topside content from model peak height to 1000 km for IRI-2020 (historical) and IRI-2026. (b) IRI-2026 bottomside minus observed bottomside, compared with GNSS-minus-hybrid content. Positive bottomside differences can offset part of a positive remaining column. Components use the primary 10 km rectangle sums. Bars show sample means. Counts refer to profiles; the full sample covers 852 dates.

3.4 Sensitivity to a common splice height

Using the observed peak as the start of the piecewise-linear IRI upper integral reduces the full-sample hybrid MAE from 5.898 to 5.558 TECU. It remains above the original IRI-2026 MAE of 5.064 TECU (Table S6). The

https://doi.org/10.5194/egusphere-2026-6656
Preprint. Discussion started: 9 November 2026
© Author(s) 2026. CC BY 4.0 License.

afternoon MAE becomes 7.703 TECU and the nighttime MAE 3.388 TECU, preserving the worsening and improvement in the respective sectors (Fig. 1a).

The same adjustment reduces the median remaining column to 3.601 TECU, with 89.1% of values positive. Aligning the integration limits reduces the remaining content, but the afternoon loss and nighttime benefit persist. Peak alignment alone therefore does not resolve the afternoon column discrepancy.

3.5 Peak-parameter differences

Figure 3 shows the conditional associations with remaining TEC. After adjustment for UTC slot, year, season, and SF morphology, observed-minus-IRI foF2 has a coefficient of 2.300 TECU per sample standard deviation (95% interval 2.088-2.511 TECU; within-model adjusted $q = 2.83 \times 10^{-100}$). The hmF2 coefficient is -0.006 TECU (95% interval -0.190 to 0.179 TECU; $q = 0.952$). Peak-frequency mismatch therefore provides a clearer association in this model than peak-height mismatch. The remaining column varies with the departure in peak-density amplitude, making that departure a useful diagnostic when the upper model is retained.

The adjusted morphology contrasts differ in direction: FSF is associated with a larger remaining column than no SF, whereas RSF and SSF have negative point estimates; the MSF interval overlaps zero. This conditional pattern differs from simply comparing the unadjusted group medians in Table 2. Local-time composition and the other covariates matter when interpreting morphology differences.

https://doi.org/10.5194/egusphere-2026-6656
Preprint. Discussion started: 9 November 2026
© Author(s) 2026. CC BY 4.0 License.

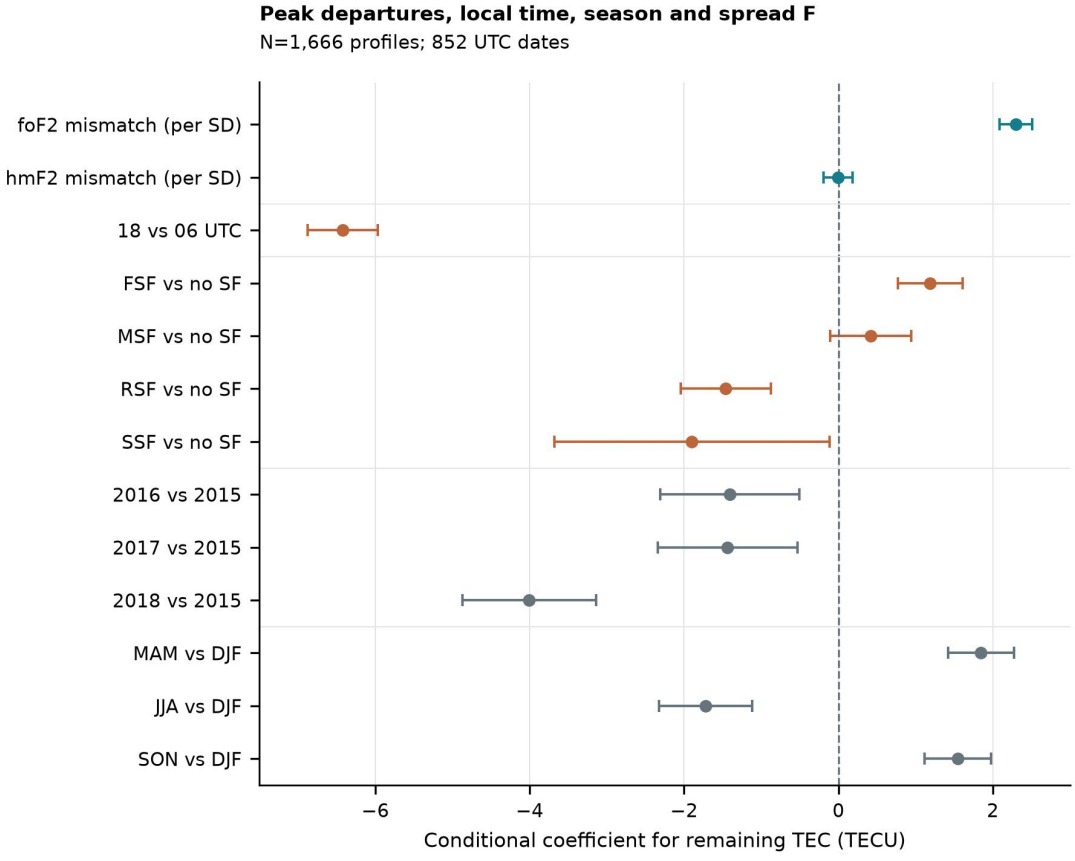


Figure 3. Non-intercept coefficients for signed remaining TEC in the IRI-2026 regression. Points and bars show estimates and pointwise 95% normal intervals using UTC-date-clustered covariance. Peak differences are observed minus model, with foF2 referenced to the quiet-background field, and are standardized by their pooled sample standard deviations. Other terms are contrasts with the stated reference categories. All terms are fitted jointly to 1,666 profiles on 852 dates. Intervals are not adjusted for multiplicity; Table S7 retains the within-model adjusted q values.

4 Discussion

4.1 Local-time dependence over Hainan

Bottomside replacement improves nighttime total-column agreement at Hainan but worsens afternoon agreement. The modeled bottomside exceeds the traced column by 4.338 TECU on average in the afternoon, whereas the nighttime difference is -0.416 TECU under the respective integration definitions. Afternoon replacement therefore removes a substantial lower contribution while leaving the model upper column unchanged. At night, the smaller lower-column difference accompanies improved agreement. The common-height comparison preserves this contrast, showing that the choice of peak boundary alone does not explain the two responses.

https://doi.org/10.5194/egusphere-2026-6656
Preprint. Discussion started: 9 November 2026
© Author(s) 2026. CC BY 4.0 License.

Zhang et al. (2006) found that ionogram-derived TEC at Hainan was generally below GPS TEC at night and above it around noon. Our combined column is also below GNSS at night, but remains below it in the afternoon, when the median difference is larger. The studies differ in their upper-profile representation, observation period, and GNSS reference product. The contrasting afternoon signs suggest that the way the upper column is estimated deserves attention alongside the local-time variation itself. Building on the Hainan column comparison and the bottomside evaluation by Wang et al. (2010), our replacement calculation shows how changing the lower contribution affects the total while the chosen upper background remains fixed.

ISR observations provide a physical basis for expecting that compatibility to vary through the day. Luan et al. (2006) found a stronger departure from a Chapman-alpha shape during daytime at Arecibo and a relationship between topside shape and peak density. Belehaki and Kersley (2006) also found that bottomside-based reconstruction represented nighttime ISR TEC better than daytime TEC. Our larger afternoon discrepancy is consistent with a more variable relation between lower-profile information and upper density decay. At Hainan, daytime fountain transport can redistribute plasma around the anomaly crest while production and loss alter the lower region (Balan et al., 2018). Temperature-dependent scale height and transport may thus change the upper content accompanying a given bottomside profile. Combining that instantaneous bottomside with a monthly upper background offers a plausible explanation for the afternoon mismatch; the ISR studies supply a physical comparison rather than a measurement of these processes at Hainan.

4.2 Total-column agreement and vertical structure

The afternoon comparison shows why a closer TEC total can accompany a lower profile that differs from the local observations. The modeled bottomside supplies more electrons than the traced bottomside under the integration definitions in Sect. 2.3. This extra content partly fills the gap between GNSS and the combined column; replacing it removes that compensation. The lower-column difference includes both density and vertical coverage. Bidaine and Warnant (2007) reported the reverse arrangement in a NeQuick case: a lower-column deficit and an upper-column excess nearly cancelled. The common lesson is that the total alone can hide component differences. At Hainan, the 4.338 TECU mean afternoon lower excess identifies the contribution whose removal accompanies the poorer total agreement.

Kutiev et al. (2012) improved TaD column agreement by adjusting the topside scale height to GNSS TEC. Here the upper profile is held fixed, and the afternoon column deteriorates after lower-profile replacement. This difference identifies the role of the component allowed to respond to observations: a measured lower column

https://doi.org/10.5194/egusphere-2026-6656
Preprint. Discussion started: 9 November 2026
© Author(s) 2026. CC BY 4.0 License.

changes how much content the upper region must supply. Our common-height result retains the afternoon deterioration, directing attention to the amount and distribution of upper content as well as the splice height.

The historical configuration comparison reinforces this interpretation. With observations fixed, the IRI-2026 upper column is smaller than the historical IRI-2020 column by 6.985 TECU in the afternoon but only 0.561 TECU at night, while pooled bottomside means remain similar. This change accounts for the larger remaining column of the IRI-2026 hybrid. The comparison identifies the upper contribution responsible for the different response to substitution. Ranking vertical accuracy would additionally require upper-profile observations, such as those used by Prol and Hoque (2021). For these Hainan observations, total-TEC agreement and agreement with the observed lower column provide complementary criteria for evaluating the model.

4.3 High-altitude content and the afternoon excess

High-altitude plasma provides an expected positive contribution to GNSS-minus-hybrid TEC because the model integral ends at 1000 km. Lee et al. (2013) found that global plasmaspheric TEC between approximately 1336 and 20200 km increased from about 2 to 4 TECU as solar activity rose toward moderate levels, with a day-night difference of about 1 TECU. The Hainan nighttime remaining median, 2.982 TECU, has a similar scale. The afternoon median, 6.861 TECU, and the same-date nighttime-minus-afternoon median, -4.091 TECU, show a larger contrast than that reported for their global upper column. The altitude ranges and spatial sampling differ, so this comparison supplies physical scale rather than a numerical upper limit.

The local component results help interpret that difference. Changing the splice and integration definition reduces the pooled remaining median from 4.287 to 3.601 TECU, and changing the retained model upper profile produces a much larger afternoon than nighttime response. These are contributions to the residual arising from the profile construction itself. High-altitude content together with a local profile mismatch offers a plausible explanation for the afternoon excess. Changes in upper-profile thickness or density decay, associated with the daytime redistribution discussed above, could enlarge that mismatch even when the lower profile is constrained.

Belehaki et al. (2004) found a morning minimum and evening maximum in GPS-minus-ionosonde content at Athens. Our afternoon and post-midnight observations sample different phases and use a different upper-profile construction. Their local-time variation supports treating the high-altitude contribution as variable, while the Hainan component comparison shows why profile compatibility must also enter the interpretation. Together these results favor using the remaining column to diagnose where additional upper-region information is needed before assigning the residual to a specific plasma reservoir.

https://doi.org/10.5194/egusphere-2026-6656
Preprint. Discussion started: 9 November 2026
© Author(s) 2026. CC BY 4.0 License.

4.4 Implications for using local observations and improving models

The Hainan comparison helps distinguish what local observations can improve from what still depends on the upper representation. Pignalberi et al. (2026) found that IRI-COR2 performed best overall at low latitude against the matched radio-occultation profiles, while near-peak overestimation remained across the tested options. They also reported better low-latitude COR2 profile agreement by day than by night. Their comparison evaluates topside densities constrained by observed peak parameters. The afternoon deterioration here concerns the change in GNSS-referenced column error after bottomside replacement. Our positive GNSS-minus-hybrid difference can coexist with such a near-peak excess because it integrates a wider altitude range. Servan-Schreiber et al. (2025) found smaller low-latitude GNSS TEC errors for NeQuick than for their COR2 combinations. These results show why a profile-based ranking does not directly determine the performance of a ground-GNSS column comparison. At Hainan, the application-relevant finding is the different response to the same bottomside substitution in the two sampled sectors.

Themens et al. (2021) obtained improved agreement with Swarm near-peak densities when observed peak height and density were supplied to E-CHAIM. In our regression, remaining TEC is associated with foF2 departures, while the conditional hmF2 coefficient is near zero. The outcomes concern different quantities: a local density responds directly to peak displacement, whereas the remaining column integrates over height and includes content above the model ceiling. Thus the Hainan result directs attention to peak amplitude and upper content for this column comparison while leaving the physical role of peak height open. Because peak density scales with foF2 squared, the positive association is consistent with amplitude changes extending into the upper region. The predictor represents departure from the quiet IRI reference, and its coefficient is used here as a diagnostic rather than an upper-profile correction.

Using local observations effectively therefore requires evaluating the lower profile and the full column together. Pignalberi et al. (2019) found that a GNSS-assisted IRI update missed the foF2 response during a storm when peak and column variations diverged. The Hainan afternoon result approaches this issue from the other direction: inserting the measured lower profile leaves the total farther from GNSS. An update should preserve the observed lower shape while adjusting the upper contribution in light of the column constraint, including content above 1000 km. Tang et al. (2022) assimilated GNSS TEC into IRI-2016 using a local ensemble Kalman filter. For applications at Hainan, the present results give a concrete evaluation criterion: check whether the afternoon column improves while retaining agreement with the measured bottomside, and assess the post-midnight result separately.

https://doi.org/10.5194/egusphere-2026-6656
Preprint. Discussion started: 9 November 2026
© Author(s) 2026. CC BY 4.0 License.

5 Scope and limitations

The conclusions concern the eligible Hainan profiles at two fixed time sectors in 2015-2018. Manual interpretation and NHPC inversion provide an observationally constrained bottomside with uncertainty, especially during spread F. Its lowest available height, the 1000 km model ceiling, and the different spatial sampling of ionosonde and GNSS affect the remaining column. The GNSS product header lists an absolute-TEC device precision of 3 TECU and a quality flag of TBD. This is an instrument specification, not an uncertainty estimate for each aggregated column or for the paired MAE difference. The header does not document the product bias-estimation algorithm or the mapping function beyond the thin-shell height. The nighttime improvement therefore describes agreement with this product; independent upper-profile information and product uncertainty characterization would be needed to assess absolute vertical accuracy.

The regression describes conditional associations within this Hainan sample. Peak parameters and bottomside content share tracing information, and the retained covariates do not separately resolve solar, geomagnetic, or transport drivers. A near-zero hmF2 coefficient therefore leaves physical height effects unresolved. The common-height calculation tests the stated integration and splice choices. Amplitude and shape changes are candidate explanations for the regional component differences.

6 Conclusions

At Hainan, replacing the IRI-2026 bottomside with a manually traced profile improves agreement with GNSS TEC after midnight but worsens it in the afternoon. Afternoon MAE increases from 6.305 to 8.440 TECU, whereas nighttime MAE decreases from 3.808 to 3.325 TECU. These opposite responses persist when the upper integral begins at the observed peak height. The usefulness of the local lower-profile constraint therefore depends on the sampled time of day when the upper background is retained.

The modeled afternoon bottomside exceeds the traced column by 4.338 TECU on average under their respective integration limits. This extra contribution partly offsets the positive GNSS-minus-combined difference, helping the original total agree more closely with GNSS. The result explains why total-column accuracy alone is insufficient for evaluating the local vertical distribution: a smaller total error can coexist with a substantial lower-column discrepancy.

The association between remaining TEC and foF2 departures provides a supporting indicator of the mismatch. For regional updating, the main implication is to evaluate the observed lower profile together with the upper content needed to account for GNSS TEC, including its greater altitude coverage. At Hainan, the afternoon

https://doi.org/10.5194/egusphere-2026-6656
Preprint. Discussion started: 9 November 2026
© Author(s) 2026. CC BY 4.0 License.

combination needs particular attention. Reporting the lower-column difference alongside the TEC error in each time sector makes the consequences of using local observations clear.

Appendix A: Additional processing and statistical details

Byte-identical duplicate daily profile files were counted once. Non-identical duplicates stopped catalogue construction. Profile eligibility required at least 20 aligned height, plasma-frequency, and density points, strictly increasing heights, finite nonnegative density, a maximum relative discrepancy of 0.015 from the frequency-density relation, and finite GNSS and model components.

Native station parameters were assigned to 15 min bins by rounding down. Numerical fields used within-bin medians; morphology used the modal class, with ties resolved by the first sorted class. The manually traced SAO profile retained its fixed UTC timestamp. Missing parameters were not interpolated. The historical GNSS field name vtec_median_center10 refers to the executed 15 min centered window specified in Sect. 2.2.

The model component sums use the 80-1000 km grid with 10 km spacing. Native IRITEC uses the 0-1000 km interval and a configured step of 0.1 km, with a 10^{-16} conversion from m^{-2} to TECU. The quiet-reference model frequency is reconstructed as $\sqrt{\mathrm{OARR}(1)/(1.24 \times 10^{10})}/\mathrm{OARR}(45)$. The density profile may include the configured storm response. The complete 50-switch configuration is listed in Table S1 of the accompanying supplement.

Bootstrap seeds are 20260809 for the overall median and 20260810 for relative MAE improvement. Both use 2,000 UTC-date clusters. Continuous regression predictors are centered and divided by their population standard deviations (ddof=0). Reference categories are 06 UTC, 2015, DJF, and no SF. DJF, MAM, JJA, and SON denote December-February, March-May, June-August, and September-November. The clustered sandwich covariance uses a finite-sample correction and normal 95% intervals. Benjamini-Hochberg adjustment includes all coefficients, including the intercept, within each of the three models. Explicit column components are excluded from the predictors to avoid direct part-whole regressions. The complete coefficient results, stratified summaries, and splice calculations are retained in the accompanying numerical tables.

Data availability

Source observations are provided by the Chinese Meridian Project through https://dcstatus.meridianproject.ac.cn/, subject to the portal's access and use conditions. The ionogram images, ionospheric parameters, GNSS vertical

https://doi.org/10.5194/egusphere-2026-6656
Preprint. Discussion started: 9 November 2026
© Author(s) 2026. CC BY 4.0 License.

absolute TEC, and RINEX records are identified by Chinese Meridian Project (n.d.-a, n.d.-b, n.d.-c, n.d.-d), respectively. These third-party records are not redistributed here.

Aggregate data for the reported figures and tables are publicly available from Science Data Bank (Wang and Wang, 2026; https://doi.org/10.57760/sciencedb.016z6), Version 1. The aggregate data and documentation are licensed under CC BY 4.0.

The deposit excludes raw observations, record-level manually traced profiles, individual manual labels and parameters, and precise observation timestamps. The authors have chosen this aggregate release scope. The files support inspection and reconstruction of the reported figures and tables, but do not permit independent repetition of the individual-profile analysis.

Code availability

The IRI-2026 Fortran distribution is available from the IRI Working Group (2026). Three MIT-licensed Python programs in the Science Data Bank deposit (Wang and Wang, 2026) redraw Figures 1-3 and export Tables 1-3 from the aggregate CSV files. The original record-level analysis code and its individual-profile inputs are not included.

Author contributions

Zheng Wang: Conceptualization; Methodology; Data curation; Formal analysis; Writing - original draft.

Quanhan Li: Formal analysis; Visualization.

Zehao Wang: Methodology; Formal analysis; Writing - review & editing.

Qinzeng Li: Methodology; Formal analysis; Writing - review & editing.

Yajun Zhu: Validation; Writing - review & editing.

Guojun Wang: Conceptualization; Data curation; Validation; Writing - review & editing.

Yusen Tian: Formal analysis; Visualization.

Xiao Wang: Resources; Data curation; Formal analysis.

Competing interests

The authors declare that they have no conflict of interest.

https://doi.org/10.5194/egusphere-2026-6656
Preprint. Discussion started: 9 November 2026
© Author(s) 2026. CC BY 4.0 License.

Acknowledgements

We acknowledge the Chinese Meridian Project (https://cstr.cn/31122.02.MSP) for the ionogram-image, ionospheric-parameter, vertical absolute TEC, and RINEX products identified by https://doi.org/10.12176/01.06.00507-V01, https://doi.org/10.12176/01.06.00508-V01, https://doi.org/10.12176/01.06.00588-V01, and https://doi.org/10.12176/01.06.00578-V01. The data portal is https://dcstatus.meridianproject.ac.cn/. We thank the project staff for their technical support and assistance with data collection. OpenAI ChatGPT and Codex were used to assist language editing, manuscript restructuring, and document consistency checks.

Financial support

This work was supported by the National Key R&D Program of China (2025YFF0510703); the Strategic Priority Research Program of the Chinese Academy of Sciences (XDA0470301); the Youth Innovation Promotion Association CAS (2023000116); the Specialized Research Fund for State Key Laboratories; and the Pandeng Program of National Space Science Center, Chinese Academy of Sciences.

References

Research and model literature

Balan, N., Liu, L., and Le, H.: A brief review of equatorial ionization anomaly and ionospheric irregularities, Earth and Planetary Physics, 2, 257-275, https://doi.org/10.26464/epp2018025, 2018.

Beggan, C. D., Kloss, C., Amblard, P., Amezza, T., Amit, H., Aubert, J., Baerenzung, J., Bregnhøj Lauridsen, J., Brown, W., Califf, S., Campuzano, S. A., Chauvet, L., Chulliat, A., Claveau, R., Coïsson, P., da Silva, M., Davies, C., Deborde, R., Dobrovolsky, M., Fillion, M., Finlay, C. C., Firsov, I., Fournier, A., Gailler, L., Gillet, N., Gomez Perez, N., Grayver, A., Gwirtz, K., Hamoudi, M., Holme, R., Holschneider, M., Hulot, G., Jager, T., Jiang, Y., Kada, M., Korte, M., Krasnoperov, R., Kuang, W., Kudin, D., Léger, J. M., Lemgharb, A., Lesur, V., Liu, P., Livermore, P. W., Madsen, F. D., Mandea, M., Matsushima, M., Matzka, J., Michaelis, I., Minami, T., Nair, M., Nakano, S., Oehler, J.-F., Olsen, N., Pavón-Carrasco, F. J., Presnyakov, S., Qian, B., Rang, X., Rogers, H. F., Rother, M., Rouxel, D., Sabaka, T., Sato, S., Saynisch-Wagner, J., Schanner, M., Serrano, M., Shakespeare-Rees, N., Shi, Y., Smith, A., Soloviev, A., Terra-Nova, F., Thebault, E., Tøffner-Clausen, L., Toh, H., Wang, J., Wardinski, I., Watson, C., Whaler, K., Xiong, C., Yan, Q., Yang, Y., Yao, H., Zeren, Z., Zhang, K., and Zhou, B.: International geomagnetic reference field: the fourteenth generation, Earth, Planets and Space, 78, 127, https://doi.org/10.1186/s40623-025-02360-0, 2026.

https://doi.org/10.5194/egusphere-2026-6656
Preprint. Discussion started: 9 November 2026
© Author(s) 2026. CC BY 4.0 License.

Belehaki, A., Jakowski, N., and Reinisch, B. W.: Plasmaspheric electron content derived from GPS TEC and digisonde ionograms, Advances in Space Research, 33, 833-837, https://doi.org/10.1016/j.asr.2003.07.008, 2004.

Belehaki, A. and Kersley, L.: Statistical validation of a technique for estimating total electron content from bottomside ionospheric profiles, Radio Science, 41, RS5003, https://doi.org/10.1029/2005RS003433, 2006.

Bidaine, B. and Warnant, R.: Assessment of the NeQuick Model at Mid-latitudes using GPS TEC and Ionosonde Data, in: First Colloquium Scientific and Fundamental Aspects of the Galileo Programme, Toulouse, France, 1-4 October 2007, https://orbi.uliege.be/handle/2268/1561, 2007.

Bilitza, D., Altadill, D., Zhang, Y., Mertens, C., Truhlik, V., Richards, P., McKinnell, L.-A., and Reinisch, B.: The International Reference Ionosphere 2012 - a model of international collaboration, Journal of Space Weather and Space Climate, 4, A07, https://doi.org/10.1051/swsc/2014004, 2014.

Bilitza, D., Pezzopane, M., Truhlik, V., Altadill, D., Reinisch, B. W., and Pignalberi, A.: The International Reference Ionosphere Model: A Review and Description of an Ionospheric Benchmark, Reviews of Geophysics, 60, e2022RG000792, https://doi.org/10.1029/2022rg000792, 2022.

Kutiev, I., Marinov, P., Fidanova, S., Belehaki, A., and Tsagouri, I.: Adjustments of the TaD electron density reconstruction model with GNSS-TEC parameters for operational application purposes, Journal of Space Weather and Space Climate, 2, A21, https://doi.org/10.1051/swsc/2012021, 2012.

Lee, H.-B., Jee, G., Kim, Y. H., and Shim, J. S.: Characteristics of global plasmaspheric TEC in comparison with the ionosphere simultaneously observed by Jason-1 satellite, Journal of Geophysical Research: Space Physics, 118, 935-946, https://doi.org/10.1002/jgra.50130, 2013.

Luan, X., Liu, L., Wan, W., Lei, J., Zhang, S.-R., Holt, J. M., and Sulzer, M. P.: A study of the shape of topside electron density profile derived from incoherent scatter radar measurements over Arecibo and Millstone Hill, Radio Science, 41, RS4006, https://doi.org/10.1029/2005RS003367, 2006.

Mannucci, A. J., Wilson, B. D., Yuan, D. N., Ho, C. H., Lindqwister, U. J., and Runge, T. F.: A global mapping technique for GPS-derived ionospheric total electron content measurements, Radio Science, 33, 565-582, https://doi.org/10.1029/97rs02707, 1998.

Pignalberi, A., Habarulema, J. B., Pezzopane, M., and Rizzi, R.: On the Development of a Method for Updating an Empirical Climatological Ionospheric Model by Means of Assimilated vTEC Measurements From a GNSS Receiver Network, Space Weather, 17, 1131-1164, https://doi.org/10.1029/2019sw002185, 2019.

https://doi.org/10.5194/egusphere-2026-6656
Preprint. Discussion started: 9 November 2026
© Author(s) 2026. CC BY 4.0 License.

Pignalberi, A., Azpilicueta, F., Nava, B., Pezzopane, M., and Bilitza, D.: Validating the International Reference Ionosphere model through altimeter-satellite vTEC observations: implications for the topside ionosphere modeling, Journal of Geodesy, 99, 81, https://doi.org/10.1007/s00190-025-02003-y, 2025.

Pignalberi, A., Haralambous, H., Bilitza, D., Coïsson, P., Nava, B., Pezzopane, M., Prol, F., Smirnov, A., Themens, D. R., and Xiong, C.: Validation of the IRI-2020 Model Topside Ionosphere Options Through COSMIC-1 and COSMIC-2 Radio Occultation Profiles Collocated With Ionosonde Observations, Space Weather, 24, e2026SW005030, https://doi.org/10.1029/2026SW005030, 2026.

Prol, F. S. and Hoque, M. M.: Topside Ionosphere and Plasmasphere Modelling Using GNSS Radio Occultation and POD Data, Remote Sensing, 13, 1559, https://doi.org/10.3390/rs13081559, 2021.

Servan-Schreiber, N., Aggarwal, M., Huang, Y., Kang, M., Shaker, A., and Bilitza, D.: Validation of the IRI-2020 model for the topside-plasmasphere using GNSS TEC measurements, Advances in Space Research, 75, 4217-4229, https://doi.org/10.1016/j.asr.2024.07.009, 2025.

Tang, J., Zhang, S., Huo, X., and Wu, X.: Ionospheric Assimilation of GNSS TEC into IRI Model Using a Local Ensemble Kalman Filter, Remote Sensing, 14, 3267, https://doi.org/10.3390/rs14143267, 2022.

Themens, D. R., Reid, B., Jayachandran, P. T., Larson, B., Koustov, A. V., Elvidge, S., McCaffrey, A. M., and Watson, C.: E-CHAIM as a Model of Total Electron Content: Performance and Diagnostics, Space Weather, 19, e2021SW002872, https://doi.org/10.1029/2021SW002872, 2021.

Wang, S. G., Shi, J. K., Wang, X., and Wang, G. J.: Validation of B2bot in the NeQuick model during high solar activity at Hainan station, Advances in Space Research, 46, 1094-1101, https://doi.org/10.1016/j.asr.2010.06.039, 2010.

Wang, G. J., Shi, J. K., Reinisch, B. W., Wang, X., and Wang, Z.: Ionospheric plasma bubbles observed concurrently by multi-instruments over low-latitude station Hainan, Journal of Geophysical Research: Space Physics, 120, 2288-2298, https://doi.org/10.1002/2014ja020245, 2015.

Wang, Z., Zhan, M., Gao, P., Wang, G., Qiu, C., Qi, Q., Shi, J., and Wang, X.: Automatic Detection and Classification of Spread-F From Ionosonde at Hainan With Image-Based Deep Learning Method, Space Weather, 21, e2023SW003498, https://doi.org/10.1029/2023sw003498, 2023.

https://doi.org/10.5194/egusphere-2026-6656
Preprint. Discussion started: 9 November 2026
© Author(s) 2026. CC BY 4.0 License.

Zhang, M.-L., Radicella, S. M., Shi, J.-K., Wang, X., and Wu, S.-Z.: Comparison among IRI, GPS-IGS and ionogram-derived total electron contents, Advances in Space Research, 37, 972-977, https://doi.org/10.1016/j.asr.2005.01.113, 2006.

Data references

Chinese Meridian Project: Ionogram Graph of Ionospheric Digital IonoSonde at Danzhou Station [data set], https://doi.org/10.12176/01.06.00507-V01, n.d.-a.

Chinese Meridian Project: Ionospheric Parameters of Ionospheric Digital IonoSonde at Danzhou Station [data set], https://doi.org/10.12176/01.06.00508-V01, n.d.-b.

Chinese Meridian Project: Ionospheric Vertical Absolute TEC of GNSS Ionospheric TEC and Scintillation Monitor at Danzhou Station [data set], https://doi.org/10.12176/01.06.00588-V01, n.d.-c.

Chinese Meridian Project: RINEX Format Parameters of GNSS Ionospheric TEC and Scintillation Monitor at Danzhou Station [data set], https://doi.org/10.12176/01.06.00578-V01, n.d.-d.

Wang, Z. and Wang, Z.: Summary data and code for afternoon and nighttime IRI-2026 electron-content partitioning over Hainan, Science Data Bank [data set and code], Version 1, https://doi.org/10.57760/sciencedb.016z6, 2026.

Software and technical documentation

Chinese Meridian Project: Product-name correspondence between Phase I and Phase II [technical documentation], https://www.meridianproject.ac.cn/dygxb/ (last access: 21 September 2026), n.d.-e.

IRI Working Group: International Reference Ionosphere IRI-2026 Fortran software distribution [software], https://irimodel.org/IRI-2026/ (last access: 8 September 2026), 2026.

UMLCAR: SAO Explorer [software documentation], https://giro.uml.edu/sao-explorer.html (last access: 21 September 2026), n.d.-a.

UMLCAR: SAO format version 4.3 [format documentation], https://ulcar.uml.edu/~iag/SAO-4.3.htm (last access: 21 September 2026), n.d.-b.